J. Fluid Mech. (2008), vol. 601, pp. 1–23. © 2008 Cambridge University Press
doi:10.1017/S0022112008000360 Printed in the United Kingdom

The pulsatile propagation of a finger of air within a fluid-occluded cylindrical tube

BRADFORD J. SMITH AND DONALD P. GAVER III
Department of Biomedical Engineering, Tulane University, New Orleans, LA 70118, USA
donald.gaver@tulane.edu

(Received 8 November 2006 and in revised form 6 December 2007)

We computationally investigate the unsteady pulsatile propagation of a finger of air through a liquid-filled cylindrical rigid tube. The flow field is governed by the unsteady capillary number $Ca_Q(t) = \mu Q^*(t^*)/\pi R^2 \gamma$, where R is the tube radius, Q^* is the dimensional flow rate, t^* is the dimensional time, μ is the viscosity, and γ is the surface tension. Pulsatility is imposed by $Ca_Q(t)$ consisting of both mean (Ca_M) and oscillatory (Ca_Ω components such that $Ca_Q(t) = Ca_M + Ca_\Omega \sin(\Omega t)$. Dimensionless frequency and amplitude parameters are defined, respectively, as $\Omega = \mu\omega R/\gamma$ and $A = 2Ca_\Omega/\Omega$, with ω epresenting the frequency of oscillation. The system is accurately described by steady-state behaviour if $Ca_\Omega < Ca_M$; however, when $Ca_\Omega > Ca_M$, reverse flow exists during a portion of the cycle, leading to an unsteady regime. In this unsteady regime, converging and diverging surface stagnation points translate dynamically along the interface throughout the cycle and may temporarily separate to create internal stagnation points at high Ω. For $Ca_\Omega < 10Ca_M$, the bubble tip pressure drop ΔP_{tip} may be estimated accurately from the pressure measured downstream of the bubble tip when corrections for the downstream viscous component of the pressure drop are applied. The normal stress gradient at the tube wall $\partial\tau_n/\partial z$ is examined in detail, because this has been shown to be the primary factor responsible for mechanical damage to epithelial cells during pulmonary airway reopening (Bilek, Dee & Gaver III 2003; Kay *et al.* 2004). In the unsteady regime, local film-thinning produces high $\partial\tau_n/\partial z$ at low Ca_Ω; however, film thickening at moderate Ca protects the tube wall from large $\partial\tau_n/\partial z$. This stress field is highly dynamic and exhibits intriguing spatial and temporal characteristics that may be used to reduce ventilator-induced lung injury.

1. Introduction

The goal of this paper is to elucidate the behaviour of the pulsatile propagation of a semi-infinite air finger through a fluid-occluded rigid circular tube. The model formulation and solution methods discussed herein may be of underlying importance to various applications including flow through porous media and the design of micro-fluidic devices. These studies may also be of importance to biological fluid mechanics applications such as pulmonary airway reopening, erythrocyte migration and embolic events in capillaries. The relevance of these studies to problems of physiological importance can is discussed in Grotberg (2001) and Gaver III *et al.* (2006).

Initial experimental investigations conducted by Fairbrother & Stubbs (1935), Bretherton (1961) and Cox (1962) of steady semi-infinite bubble propagation through a rigid tube demonstrated a correlation between residual film thickness far upstream of the bubble h_o^* and the dimensionless fluid capillary number $Ca = \mu U^*_{AVG}/\gamma$. Ca is a function of fluid viscosity (μ), surface tension (γ), and the average fluid velocity downstream of the bubble tip U^*_{AVG}; representing the balance of viscous and surface-tension-induced forces. Bretherton extended experimental results to the limit of vanishing Ca via matched asymptotic analysis, determining that $\lim_{Ca\to 0} h^*_0 \propto Ca^{2/3}$. Park & Homsy (1984) followed Bretherton's groundbreaking work to formalize the low Ca asymptotic analysis with perturbation theory. Ratulowski & Chang (1989) used an arclength-angle formulation of a composite lubrication equation to extend the asymptotic analysis to higher Ca.

We simulate this system to capture the complex interfacial and flow-field dynamics. Mesh-based computational studies using finite-difference routines (Reinelt & Saffman 1985; Wassmuth, Laidlaw & Coombe 1993) and the finite-element method (Shen & Udell 1985; Giavedoni & Saitia 1997; Heil 2001) have been successfully employed under steady-state conditions. Application of the boundary-element method (BEM), our chosen technique, to air finger propagation in channels was pioneered by Lu & Chang (1988) and followed by Ingham, Ritchie & Taylor (1992) and Halpern & Gaver III (1994). This computational technique was selected because of the inherent efficiency of the method, which requires meshing and computations only at node points along the boundary of the domain. With axial symmetry and the addition of lubrication theory approximations in the thin-film region, where the BEM is computationally demanding, computational costs for the time-dependent simulation are tractable.

Our interest in oscillatory propagation of a semi-infinite finger of air stems from its importance in understanding the reopening of collapsed pulmonary airways, since airway reopening can damage the sensitive epithelial cells that line these airways and contribute to ventilator-induced lung injury (VILI). This phenomenon has been experimentally and computationally investigated under steady-reopening conditions in flexible-walled systems (Gaver III *et al.* 1990, 1996; Yap *et al.* 1994; Perun & Gaver III 1995*a*, *b*; Yap & Gaver III 1998; Heil 2000; Hazel & Heil 2003, 2006; Juel & Heap 2006). In addition, rigid-walled systems have been used to investigate surfactant effects (Ghadiali, Halpern & Gaver III 2001; Ghadiali & Gaver III 2003). Important studies related to liquid plug motion with and without surfactant have been published by Fujioka & Grotberg (2004, 2005). To date, the exploration of pulsatile reopening has been limited to a two-dimensional channel flow (Zimmer, Williams & Gaver III 2005) who investigated the flow fields and transport of a surface-inactive contaminant (aka 'surfinactant'). In the present analysis we consider pulsatile flow through a cylindrical tube, and focus our analysis on the resulting normal-stress gradients that have been shown to damage epithelial cells (Bilek *et al.* 2003; Kay *et al.* 2004).

In § 4, we investigate the following characteristics: the dimensionless bubble tip pressure drop ΔP_{tip}, extrapolated ΔP_{tip} (defined below), curvature κ_{tip}, velocity U_{tip}, and upstream bubble radius β. We consider the time-dependent behaviour of these properties and explore the trends that occur at fixed mean capillary number Ca_M and oscillatory amplitude A over a range of dimensionless frequencies Ω. In § 5, we explore the implications of these flows on the temporally and spatially dependent normal stress gradient $\partial\tau_n/\partial z$, because this mechanical stress component has been shown to be of fundamental importance to the damage of pulmonary epithelial cells that may relate to ventilator-induced lung injury (Gaver III *et al.* 2006).

2. Problem formulation

We examine the oscillatory progression of a semi-infinite finger of air through a rigid cylindrical tube of radius R containing a Newtonian fluid of viscosity μ and

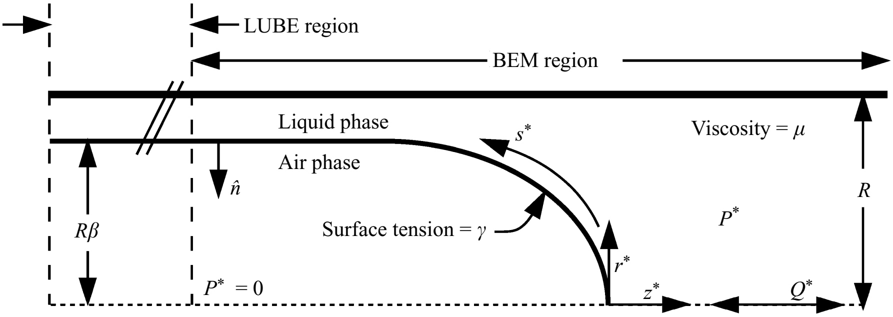

FIGURE 1. Model.

a constant surface tension γ (figure 1). The dynamics of the air phase are neglected and the reference pressure in this region is $P^* = 0$. We model this system using cylindrical coordinates and assume symmetry about the z-axis; positions are fully defined by an axial position z^* and a radial position r^* ($\boldsymbol{r}^* = (r^*, z^*)$). s^* defines the arclength coordinate along the air–liquid interface, originating at the bubble-tip and spanning through the boundary-element method (BEM) and lubrication theory (LUBE) regions.

Bubble motion is induced by downstream flow, dictating the behaviour of the air finger by conservation of mass. The downstream flow rate ($Q^*(t^*)$) is defined according to (2.1), consisting of mean (Q^*_M) and oscillatory (Q^*_ω) components.

$$Q^*(t^*) = Q^*_M + Q^*_\omega \sin(\omega t^*). \tag{2.1}$$

The dimensional frequency ω determines the period of oscillation. The reopened region far upstream of the bubble tip is of radius $r^*_{men} = R\beta$. Since the interface is a free surface, β is determined as part of the solution.

2.1. *Governing equations, BEM region*

Governing equations for fluid motion are scaled using the parameters shown in (2.2), with dimensional quantities denoted with an asterisk (*).

$$\left.\begin{aligned} u^*_z = Uu_z = \left(\frac{\gamma}{\mu}\right) u_z, \quad u^*_r = \left(\frac{\gamma}{\mu}\right) u_r, \quad r^* = Rr, \quad z^* = Rz, \quad r^*_{men} = Rr_{men}, \\ P^* = \frac{\gamma}{R} P, \quad t^* = \left(\frac{R\mu}{\gamma}\right) t, \quad \kappa^* = \frac{1}{R}\kappa, \quad \tau^* = \frac{\gamma}{R}\tau. \end{aligned}\right\} \tag{2.2}$$

The velocity scale $U = \gamma/\mu$, a balance between surface tension and viscous forces, represents the interfacial relaxation velocity. All lengths are scaled by the tube radius R, and time is scaled naturally with velocity and length. The law of Laplace is used to scale all stresses. We pose the governing equations and boundary conditions in the laboratory frame of reference. The time-stepping algorithm described below (§ 3.4, § 3.5) allows the simulations to focus on the bubble tip region of interest.

We assume inertial effects are negligible and the unsteadiness in the problem arises purely from the kinematic boundary condition (limitations associated with this assumption are addressed in § 6). The flow field is thus described by the dimensionless Stokes equation (2.3) and continuity equation (2.4).

$$\nabla P = \nabla^2 \boldsymbol{u}, \tag{2.3}$$

$$\nabla \cdot \boldsymbol{u} = 0. \tag{2.4}$$

The flow is driven far downstream with an imposed velocity profile

$$\left.\begin{aligned} u_r(r,t) &= 0,\\ u_z(r,t) &= 2Ca_Q(t)(1-r^2). \end{aligned}\right\} \tag{2.5}$$

Scaling (2.1) yields the dimensionless downstream flow rate

$$Ca_Q(t) = Ca_M + Ca_\Omega \sin(\Omega t). \tag{2.6}$$

The dimensionless parameters describing the system are:

$$Ca_Q(t) = \frac{\mu U^*_{AVG}(t^*)}{\gamma} = \frac{\mu Q^*(t^*)}{\pi R^2 \gamma}, \quad \Omega = \frac{\mu \omega R}{\gamma}, \quad A = \frac{2Ca_\Omega}{\Omega}. \tag{2.7}$$

$Ca_Q(t)$ is a capillary number that represents the balance between viscous and surface tension effects, consisting of mean (Ca_M) and sinusoidal oscillatory (Ca_Ω) components. $U^*_{AVG}(t)$ represents the average velocity across a cross-section in the downstream region, equal to $Q^*(t)/\pi R^2$. By conservation of mass, $Q^*(t)$ also represents the gas flow rate into the finger of air from the upstream end. The dimensionless frequency (Ω) and amplitude (A) parameterize the bubble oscillation. A represents the peak-to-peak oscillatory stroke length of the bubble tip; the bubble tip oscillates with a stroke length $L_{stroke} = A\overline{\beta}R$, where $\overline{\beta}$ is the cycle-averaged bubble radius that exists far upstream of the bubble tip after all capillary waves are dampened. $\overline{\beta}$ is calculated by global conservation of mass as follows:

Flow through the upstream (z_{LFT}) and downstream (z_{RT}) boundaries is

$$\bar{Q}^*_{LFT} = \pi\bar{\beta}^2 R^2 \bar{U}_{tip}, \; \bar{Q}^*_{RT} = \pi R^2 Ca_M, \tag{2.8}$$

which must be equal because both the air and liquid phases are considered incompressible. Therefore,

$$\bar{\beta} = \sqrt{Ca_M/\bar{U}_{tip}}. \tag{2.9}$$

In our simulations we impose A,and hence L_{stroke} and $\bar{\beta}$ are determined as part of the solution.

No slip and no penetration are enforced at the tube wall:

$$\boldsymbol{u}(\boldsymbol{r},t)|_{r=1} = 0. \tag{2.10}$$

The interfacial stress jump condition is defined as

$$[\boldsymbol{\sigma}\cdot\hat{\boldsymbol{n}}_{men}] = -\kappa\hat{\boldsymbol{n}}_{men} \tag{2.11}$$

where $\boldsymbol{\sigma}$ is the stress tensor for the viscous occluding fluid, $\hat{\boldsymbol{n}}_{men}$ is the outward facing interfacial normal vector, and κ is the three-dimensional interfacial curvature.

2.2. *Governing equations, LUBE region*

In the region of the model governed by lubrication theory (LUBE regions denoted in figures 1 and 2), the evolution equation for the radial position of the meniscus (2.15) is obtained from the z-component of the Stokes equation. We simplify by assuming radial symmetry (as in the BEM region), viscous dominated flow, and that the ratio of radial to axial length scales is small following a long-wavelength approximation

$$\frac{\partial P^*}{\partial z^*} = \mu\left(\frac{1}{r^*}\frac{\partial}{\partial r^*}\left(r^*\frac{\partial u^*_z}{\partial r^*}\right)\right). \tag{2.12}$$

Integrating (2.12) twice with respect to r, applying the boundary conditions $\partial u^*_z/\partial z^*|_{r^*=r^*_{men}} = 0$ and $u^*_z|_{r^*=R} = 0$, then scaling with (2.2) yields the axial velocity

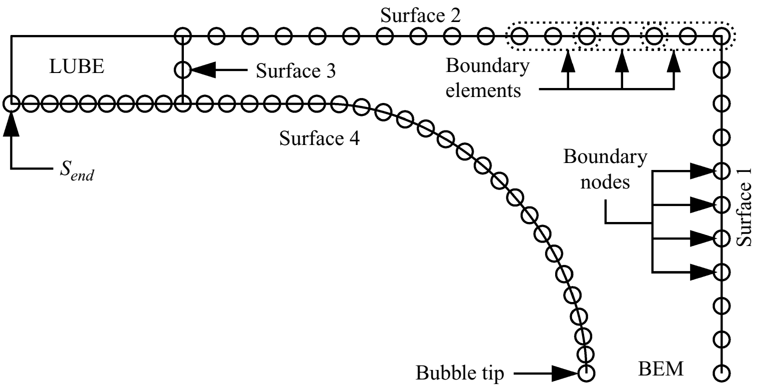

FIGURE 2. Computational domain.

in the lubrication region:

$$u_z = \frac{\kappa_z}{2Ca_Q(t)}\left(\frac{r^2-1}{2} - r_{men}^2\ln(r)\right), \tag{2.13}$$

where κ_z is the curvature derivative in the z-direction. We integrate the velocity over the cross-sectional area of the fluid to determine the flow rate Q, from which we attain the flow derivative in the z-direction $\partial Q/\partial z$.

Differentiating Q with respect to z produces the relationship between the evolution equation and the flow derivative

$$\frac{\partial r_{men}}{\partial t} = \frac{1}{2\pi r_{men}}\frac{\partial Q}{\partial z}, \tag{2.14}$$

into which we substitute $\partial Q/\partial z$ to obtain the evolution equation in the lubrication region

$$\begin{aligned}\frac{\partial r_{men}}{\partial t} = \left(\frac{1}{16 r_{men}}\right)\Bigg[&\kappa_z\left(8r_{men}\frac{\partial r_{men}}{\partial z} - 8r_{men}^3\frac{\partial r_{men}}{\partial z} + 16\ln[r_{men}]r_{men}^3\frac{\partial r_{men}}{\partial z}\right)\\ &+\kappa_{zz}\left(-1+4r_{men}^2-3r_{men}^4+4\ln[r_{men}]r_{men}^4\right)\Bigg].\end{aligned} \tag{2.15}$$

It should be noted that if the bubble speed varies too rapidly, spatial gradients in film thickness will be created that may violate the implicit lubrication approximation long-wavelength approximation. The influence of these errors on the bubble tip region of interest (modelled using the BEM formulation) was found to be negligible when the lubrication region is introduced far upstream of the bubble tip.

3. Method of solution

While the problem formulation provided above is posed in the laboratory frame of reference, simulation in this frame would result in an intractably long domain when solved over a long time duration. For this reason, while the governing equations are solved in the laboratory frame, we kinematically translate the solution to the bubble tip frame of reference as described in § 3.4. The boundary-element method (BEM) is used to determine the flow field in the region of the model surrounding the bubble tip (figures 1 and 2). A description of the BEM is available in Appendix A.

3.1. *Boundary conditions: BEM region*

As described in Halpern & Gaver III (1994) and Zimmer *et al.* (2005), boundary conditions must be carefully identified to generate accurate results. This entails the definition of mixed conditions at the corner points as described in Appendix B. Flow through the downstream surface of the model (surface 1 in figure 2) is defined by the instantaneous capillary number $Ca_Q(t)$ (2.6). Along the tube wall, no slip and no penetration are enforced *via* velocity conditions. At the interface (surface 4 in figure 2), τ_r and τ_z are obtained from (2.11). For a complete description of the boundary conditions in the BEM domain see table 1 in Appendix B.

3.2. *Lubrication theory*

Lubrication theory is used to describe the flow field in the upstream region of the model, reducing the length of the BEM domain and providing boundary conditions on the adjacent BEM region (figure 2, surface 3). The curvature κ_z and the curvature spatial derivatives κ_z and κ_{zz} are continuous throughout the BEM and LUBE regions of the model owing to the implementation of a master surface spanning the length of the domain.

3.3. *Boundary conditions: LUBE region, BEM/LUBE boundary*

In the LUBE region, nodes are fixed axially; the radial velocity is defined by the evolution equation (2.15). Connection of the two domains through the master cubic spline and the shared boundary condition produces a continuous description of the flow field and interfacial behaviour. At the boundary between the BEM and LUBE regions, axial velocity and radial stress conditions are enforced. As at the downstream end of the BEM region, shear stress is defined on the corner nodes by differentiating the velocity profile.

3.4. *Kinematic translation, tip frame of reference*

Solution of the boundary integral equations for a given time step produces interfacial velocities; the motion of the interface is governed by the kinematic boundary condition that is applied to the free surface. To prevent elongation of the computational domain, nodes are kinematically translated in the bubble tip frame of reference by subtracting the tip velocity from the axial velocity at each node point. This allows the tip of the bubble to remain fixed at the origin while solving the equations of motion in the laboratory frame of reference. In the BEM region we apply the following condition:

$$\frac{\mathrm{d}\boldsymbol{M}}{\mathrm{d}t} = [(u_z - u_{tip})n_z + u_r n_r]\hat{\boldsymbol{n}}, \tag{3.1}$$

where $\boldsymbol{M} = (r_m(s,t), z_m(s,t))$ is the interfacial position vector. Details of this technique are provided by Zimmer *et al.* (2005). Likewise, in the lubrication region we apply

$$u_r^{interface} = \left(\frac{\partial r_{men}}{\partial t} - u_{tip} n_z\right) n_r \tag{3.2a}$$

$$u_z^{interface} = 0 \tag{3.2b}$$

3.5. *Time stepping*

The time-dependent evolution of the meniscus and flow field is determined by the NetLib routine DLSODES (double precision Livermore solver for ordinary differential equations with general sparse Jacobian matrices), operating on a master domain spanning the BEM and LUBE regions. Nodal positions are redistributed every quarter cycle, with increased nodal density in the tip region.

3.6. *Convergence*

The solution convergence is assessed by investigating the impact of critical properties of our solutions (bubble tip pressure drop ΔP_{tip}, bubble tip curvature κ_{tip}, tip velocity U_{tip}) as a function of the nodal density and extent of the boundary-element domain. Nodal density on the free surface was determined by iterating the steady-state solution of $Ca(t) = 0.1$ with an increasing number of interfacial nodes. The interfacial nodal density (40 elements) was deemed to provide sufficient accuracy because the doubling of the number of elements resulted in a maximum change in the solution variables $(\bar{\beta}, \Delta P_{tip}, U_{tip}, \kappa)$ of less than 5×10^{-4}. Comparison of steady-state results over $0.01 < Ca_Q < 1.3$ with the simulations of Reinelt & Saffman (1985) show a maximum difference in predicted film thickness <0.5 % and bubble tip pressure drop <1.6 %, demonstrating excellent agreement between the two methods.

The normal component of the interfacial velocity in the tip frame of reference was used to define convergence in steady-state simulations. When the maximum normal velocity throughout the BEM and LUBE regions was less than 5×10^{-8}, the steady-state solution was considered converged. Convergence in oscillatory simulations was determined by comparing results from previous cycles. ΔP_{tip}, κ_{tip}, and U_{tip} were compared at 144 temporal points per cycle; when the maximum difference of these characteristics varied by less than 10^{-5} between consecutive cycles, the oscillatory simulation was considered converged.

In order to determine the appropriate domain length for the BEM region, solutions were calculated for BEM regions over $z_{LFT} < z < z_{RT}$, where z_{LFT} defines the juncture between the BEM region and the thin-film region that is modelled using lubrication approximations, and z_{RT} is the downstream extent of the BEM domain (typically, $z_{RT} = 3$). Solutions for $A = 1$, $Ca_M = 0.01$, $\Omega = 0.06$ were calculated with the length of the domain ranging over $-14 < z_{LFT} < -0.6$ with a fixed nodal density. Bubble tip parameters ΔP_{tip}, U_{tip} and κ_{tip} were insensitive to z_{LFT} for $z_{LFT} < -3$, solutions were therefore calculated with the BEM region over $-4 < z < 3$.

4. Results

4.1. *Flow field*

As a baseline, we consider the flow field occurring at $Ca_M = 0.01$, $\Omega = 0.04$, $A = 5$. In figure 3 the dynamic nature of the flow field is demonstrated by time-dependent streamlines at points throughout the oscillatory cycle. As such, figures 3(*a*)–3(*f*) present instantaneous streamlines every one-sixth of a cycle, and identify the time-dependent locations of converging (+) and diverging (−) surface stagnation points as well as an internal stagnation point (×) that temporarily exists during deceleration. These stagnation points are emphasized because of their importance in interfacial transport (Stebe & Maldarelli 1994; Stebe & Barthès-Biesel 1995; Zimmer *et al.* 2005). Internal stagnation points such as those observed in this study have been predicted to exist in steady flows by Rame (2007) under conditions when film thickening exists. Note that since this is an unsteady flow, the interface is not a streamline and therefore streamlines may intersect the free surface.

Figure 3(*a*) shows flows that exist at $Ca_Q = Ca_M$ in the accelerating phase, producing a converging surface stagnation point (+) at the bubble tip and a diverging surface stagnation point (−) in the transition region between the bubble tip to the thin-film (similar to steady-state flows). As the flow rate is increased to a maximum of $Ca_Q(t) = Ca_M + Ca_\Omega$ (figure 3*a*, *b*) the transition region diverging surface stagnation

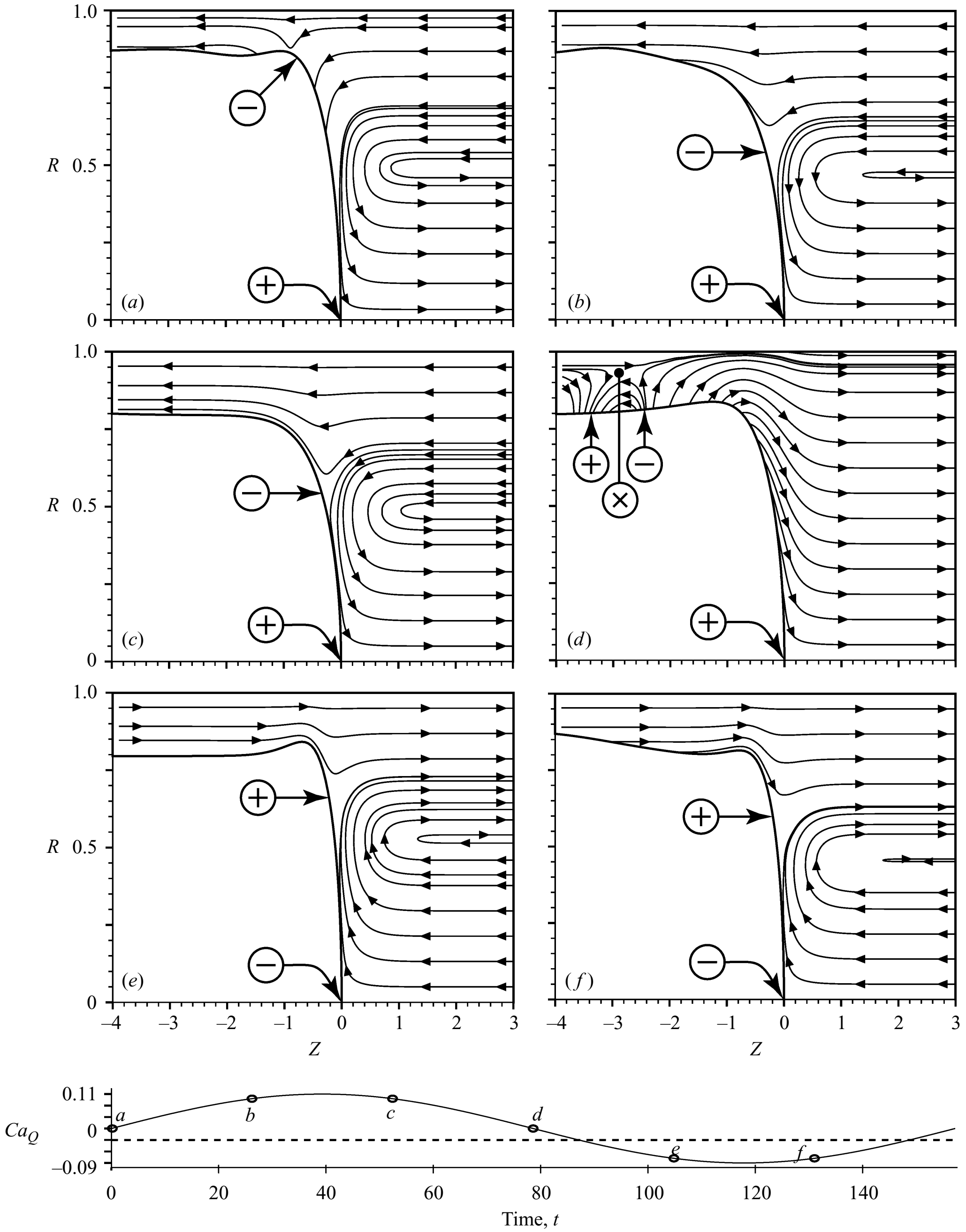

FIGURE 3. Instantaneous streamlines, bubble tip frame of reference. $Ca_M = 0.01$, $\Omega = 0.04$, $A = 5$, $Ca_\Omega = 0.1$. Converging surface stagnation points are represented with (+), diverging surface stagnation points with (−), and interior stagnation points separated from the interface are indicated with (×).

point (−) migrates towards the bubble tip. Subsequently, as $Ca_Q(t)$ decreases towards Ca_M (figure 3*c*, *d*), the transition region surface stagnation point migrates along the interface away from the bubble tip, eventually separating from the free surface to create a stagnation point in the bulk fluid (denoted by × in figure 3*d*) and ultimately dissipating at the wall. It is important to note the dissimilarities between figures 3(*a*) and 3(*d*). While both of these flows occur at $Ca_Q(t) = Ca_M$ – unlike the accelerating phase, the decelerating phase bears little similarity to the steady-state flow field that would exist at Ca_M, as it includes two converging surface stagnation points in addition to the internal stagnation point. This behaviour clearly demonstrates that the time-dependent nature of the system modifies the interfacial geometry and flow field even though inertia is neglected in this model. In addition, the internal stagnation point was not observed in prior two-dimensional planar investigations of pulsatile flow (Zimmer *et al.* 2005), highlighting the importance of geometry on the flow fields.

When flow reversal occurs ($Ca_Q(t) < 0$), the surface stagnation points change polarity with the bubble tip transforming from convergent (+) to divergent (−), and the transition region surface stagnation point becoming convergent (figure 3*e*, *f*). With increasing Ω, the reverse-flow transition region surface stagnation point (+) may also separate from the interface and convect into the bulk of the fluid. A capillary wave is seen travelling in the $-z$-direction in (figure 3*e*, *f*), as discussed by Fujioka & Grotberg (2004, 2005). The local film thinning occurring in the accelerating phase of the reverse stroke (figure 3*e*) plays a significant role in the normal stress gradient $\partial\tau_n/\partial z$, this effect is discussed in § 5.1.

4.2. *Hysteresis loops*

Figure 4 presents hysteresis loops that demonstrate the dynamic relationship between the key system responses ΔP_{tip}, extrapolated ΔP_{tip}, κ_{tip} and $Ca_Q(t)$. The extrapolated ΔP_{tip}, $(\Delta P_{tip})_{ext}$, is determined from the pressure at the downstream boundary by subtracting the instantaneous Poiseuille flow viscous pressure drop $P_\mu = 8L_{DOWN}Ca_Q(t)$ that occurs between bubble tip and the downstream end of the domain, $L_{DOWN} = z_{RT}$. Practically, $(\Delta P_{tip})_{ext}$ is an important quantity because this characteristic is measurable experimentally, whereas it is not possible to directly measure ΔP_{tip}. We therefore seek to determine whether $(\Delta P_{tip})_{ext}$ is an adequate measure of the tip pressure drop.

Figure 4(*a*) shows hysteresis loops of ΔP_{tip} and $(\Delta P_{tip})_{ext}$ over one cycle for $Ca_M = 0.01$, $A = 5$ and $\Omega = 0.04$. $(\Delta P_{tip})_{ext}$ follows the same qualitative pattern as ΔP_{tip}, indicating that downstream pressure measurements can be used to evaluate interfacial pressure jumps experimentally (a cycle-averaged quantitative comparison is provided below). In the region $Ca_Q(t) \geqslant Ca_M$, the hysteresis loop rotates in the counterclockwise direction, and ΔP_{tip} increases with $Ca_Q(t)$ so that ΔP_{tip} is greater on the deceleration phase. Streamlines corresponding to this behaviour are shown in figure 3(*a*–*d*), which correspond to the points *a*–*d* in figure 4. We find that at large Ca_M or small A, the entire hysteresis loop rotates in the counterclockwise direction. However, as shown in figures 3 and 4, for small Ca_M or large A the hysteresis loops cross in the reverse flow region ($Ca_Q < 0$, points *e* and *f*). This results in a portion of the hysteresis loop that rotates in the clockwise direction. Note that the large A is critical to this behaviour, as it allows for a significant region of film thickening during the cycle. For example, if we fix $Ca_\Omega = A\Omega/2$ by decreasing A and increasing Ω then the hysteresis area increases and the cross-over region is eventually eliminated.

In order to fully understand the behaviour of ΔP_{tip}, it is instructive to investigate the dynamic tip curvature, κ_{tip} (figure 4*b*). Clearly, ΔP_{tip} is consistent with κ_{tip} – this occurs because curvature is a major component of the interfacial stress condition (2.11); qualitative differences arising between κ_{tip} and ΔP_{tip} are a result of viscous effects that become more significant as Ω is increased. In the forward portion of

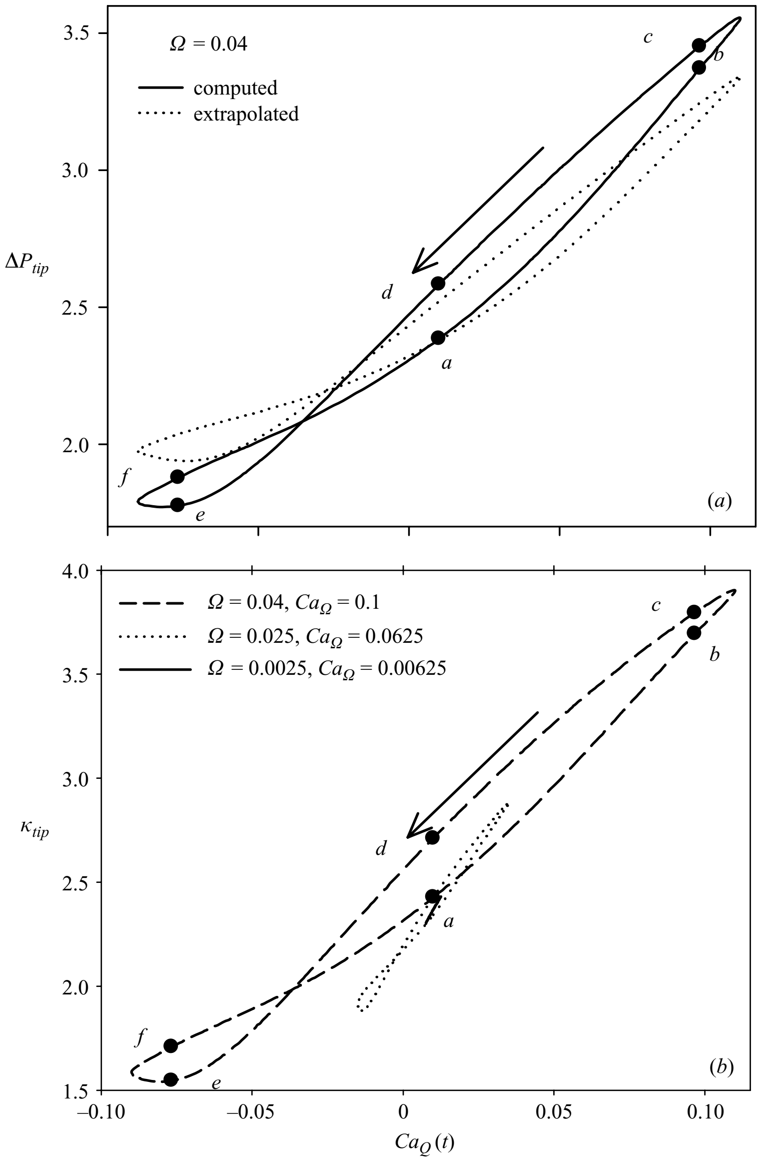

FIGURE 4. Bubble tip pressure drop ΔP_{tip} (*a*) and curvature κ_{tip} (*b*) hysteresis loops for $Ca_M = 0.01$, $\mathrm{A} = 5$. Symbols *a*–*f* correspond to streamlines shown in figure 3.

the oscillatory cycle, κ_{tip} increases with increasing $Ca_Q(t)$ until the maximum velocity ($Ca_Q = Ca_M + Ca_\Omega$) is reached. Subsequent deceleration results in local film thickening that increases the tip curvature (compare figure 3*a* to figure 3*d*) and, hence, increases ΔP_{tip}. This behaviour results in the counterclockwise direction of the hysteresis loop.

The clockwise rotation of the ΔP_{tip} and κ_{tip} hysteresis loops occurs in the portion of the cycle where $Ca_Q(t) < 0$ when A is large (see above). The κ_{tip} response shows that the curvature is reduced as the bubble travels in the $-z$-direction (which results in the blunting of the bubble tip), causing a commensurate decrease in ΔP_{tip}. κ_{tip} (and hence ΔP_{tip}) increases in the accelerating phase near the minimum velocity (compare figure 3*e* to figure 3*f*), yielding the clockwise orientation.

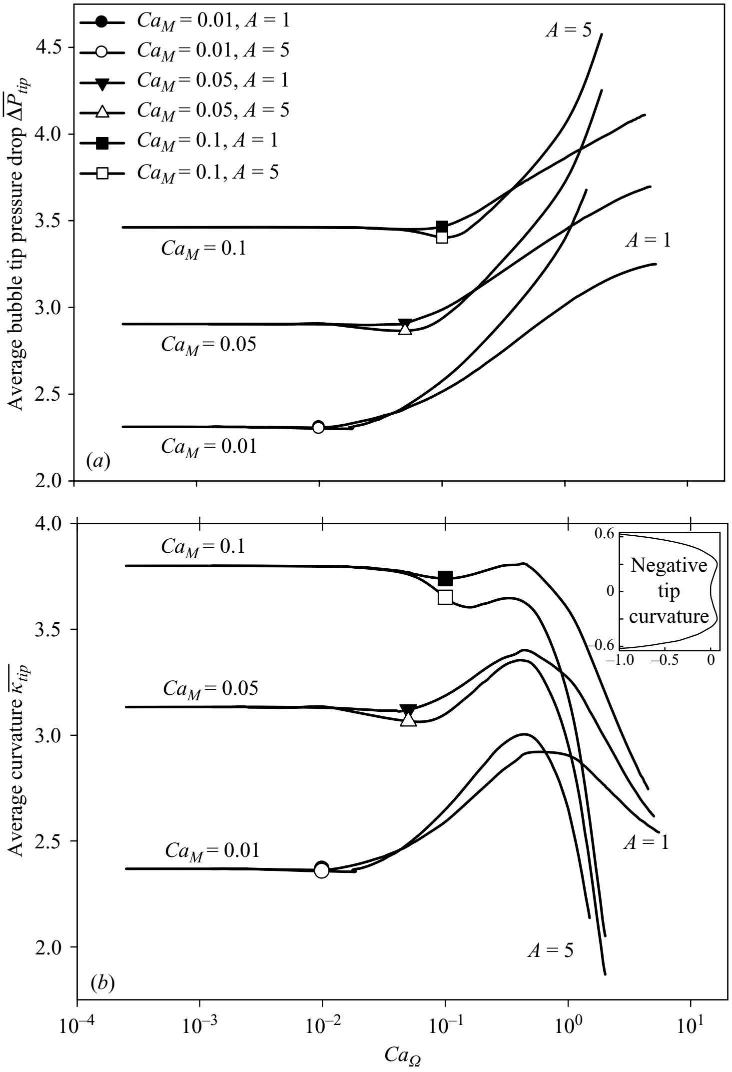

FIGURE 5. Cycle averaged bubble tip pressure drop $\Delta\bar{P}_{tip}$ (*a*) and curvature $\bar{\kappa}_{tip}$ (*b*). Symbols indicate the dimensionless frequency where $Ca_\Omega = Ca_M$, data to the right-hand side of the symbols indicate the unsteady regime and the presence of reverse flow. Inset region is representative of the interfacial geometry when $\kappa_{tip} < 0$.

4.3. *Cycle-averaged results*

To elucidate the trends present over the range of parameters considered herein ($Ca_M = 0.01, 0.05, 0.1$; $A = 1, 5$ and $5 \times 10^{-4} \leqslant \Omega \leqslant 10$), we present the cycle-averaged results in figures 5 to 7. Generally, when $Ca_\Omega < Ca_M$, quasi-steady behaviour is observed and when $Ca_\Omega > Ca_M$, the cycle-averaged data are modified from the steady-state response. This modification results from the reverse flow that exists during a portion of the cycle when $Ca_\Omega > Ca_M$; we term this the *unsteady regime.*

At low Ca_M (< 0.1), in the unsteady regime the cycle-averaged bubble tip curvature $\bar{\kappa}_{tip}$ (figure 5*b*) initially increases with Ca_Ω. This increase in $\bar{\kappa}_{tip}$ is consistent with the hysteresis loops shown in figure 4(*b*), which clearly demonstrates that an increase

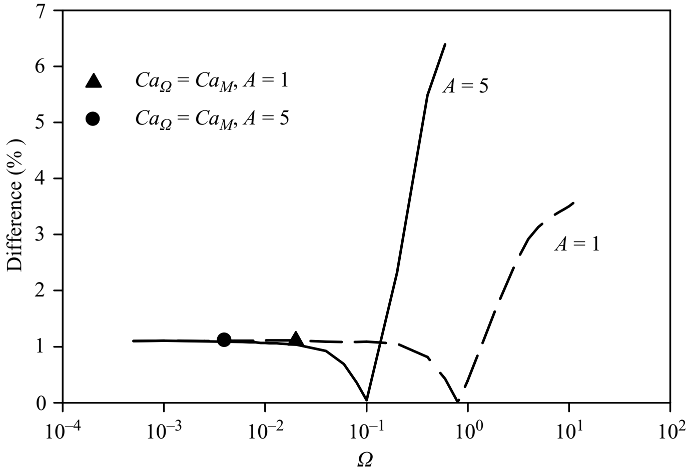

FIGURE 6. Percentage difference between the cycle-averaged pressure drop $\Delta\bar{P}_{tip}$ and extrapolated $\Delta\bar{P}_{tip}$ for $Ca_M = 0.01$. Data to the right-hand side of the symbols indicate the unsteady regime and the presence of reverse flow.

in Ca_Ω leads to a net upward shift of the hysteresis loops. Subsequently, figure 5(*b*) demonstrates that a further increase in Ca_Ω yields a precipitous reduction in $\bar{\kappa}_{tip}$. This behaviour occurs because κ_{tip} becomes negative for a portion of the oscillatory cycle (see inset of figure 5*b*); meanwhile, κ_{tip} during the large Ca_Q forward stroke approaches a constant (Halpern & Gaver III 1994). As a result, $\bar{\kappa}_{tip}$ is reduced. As A is increased, the reduction in $\bar{\kappa}_{tip}$ is more abrupt because the bubble tip becomes inverted for an extended period of the cycle.

As with $\bar{\kappa}_{tip}$, the cycle-averaged bubble tip pressure drop $\Delta\bar{P}_{tip}$ (figure 5*a*) is unaffected by frequency unless reverse flow occurs ($Ca_\Omega > Ca_M$). In this unsteady regime, $\Delta\bar{P}_{tip}$ exhibits a monotonic increase, with $\Delta\bar{P}_{tip}$ initially increasing in concert with $\bar{\kappa}_{tip}$. This correlation between $\Delta\bar{P}_{tip}$ and $\bar{\kappa}_{tip}$ is consistent with the hysteresis loops shown in figure 4. However, at high Ca_Ω this correlation is broken and $\Delta\bar{P}_{tip}$ increases while $\bar{\kappa}_{tip}$ decreases. This occurs because of the increasing effect of viscous forces as velocity increases, as described in § 4.2.

To assess the accuracy of $(\Delta\bar{P}_{tip})_{ext}$ as an estimate of $\Delta\bar{P}_{tip}$ as discussed above, we compare $\Delta\bar{P}_{tip}$ to $(\Delta\bar{P}_{tip})_{ext}$ in figure 6. This comparison demonstrates that $(\Delta\bar{P}_{tip})_{ext}$ may be used to predict $\Delta\bar{P}_{tip}$ at Ca_Ω well within the unsteady regime. In fact, our calculations show that the deviation is very low (less than 1%) when $\Omega < 1$ for $A = 1$ or $\Omega < 0.1$ for $A = 5$ with $Ca_M = 0.01$. This large range of correlation holds true for all Ca_M considered in this study, indicating that one may confidently use $(\Delta\bar{P}_{tip})_{ext}$ to estimate $\Delta\bar{P}_{tip}$ when $Ca_\Omega < 10Ca_M$.

Figure 7(*a*) shows that $\Delta\bar{U}_{tip}$ increases significantly with increasing Ca_Ω. At $A = 1$, $\Delta\bar{U}_{tip}$ stabilizes at high frequencies to a value independent of Ω, but decreases with Ca_M. Similar trends exist for $A = 5$; however, direct observations of the plateau region were not feasible. Figure 7(*b*) shows a commensurate decrease in cycle-averaged bubble half width $\bar{\beta}$ (as defined in § 2.1) with increasing Ca_Ω. Obviously, pulsatile flow results in a net film thickening, which is observable in figure 3. As expected, this film thickening response occurs largely in the unsteady regime and is related to the increasing film thickness that is observed under high-*Ca* steady propagation (Halpern & Gaver III 1994). The effects of bubble thickening are far more pronounced

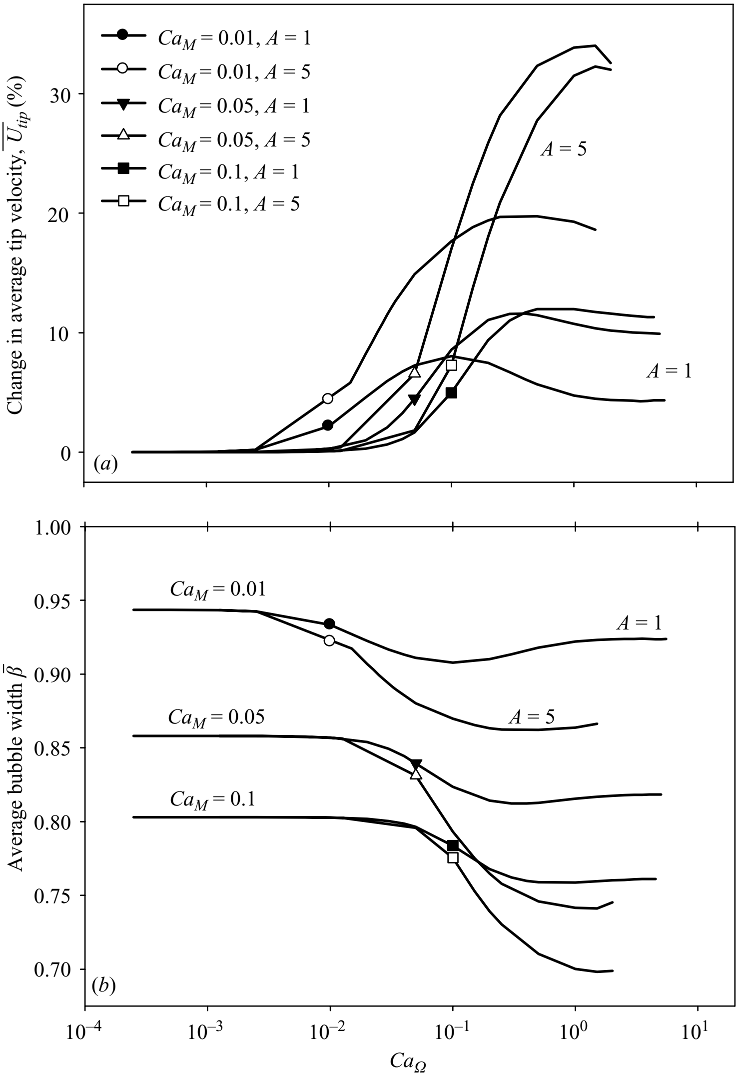

FIGURE 7. Cycle averaged percentage change in bubble tip velocity $\Delta\bar{U}_{tip}$ (a) and bubble half-width $\bar{\beta}$ (b). Symbols indicate the dimensionless frequency where $Ca_\Omega = Ca_M$, data to the right-hand side of the symbols indicate the unsteady regime and the presence of reverse flow.

with increasing A because high-amplitude cycling modifies the bubble geometry over a region that extends far upstream of the bubble tip. In contrast, low A perturbs the geometry only in the immediate vicinity of the tip and thus does not greatly modify the residual film deposited on the wall.

5. Mechanical stresses

Above, we have discussed the behaviour of the flow field and bubble-tip properties (U_{tip}, ΔP_{tip}, κ) that are important for understanding the fluid mechanical interactions fundamental to this analysis. These fundamental characteristics are clearly modified by the presence of pulsatile flow, especially when reverse-flow conditions exist. In this

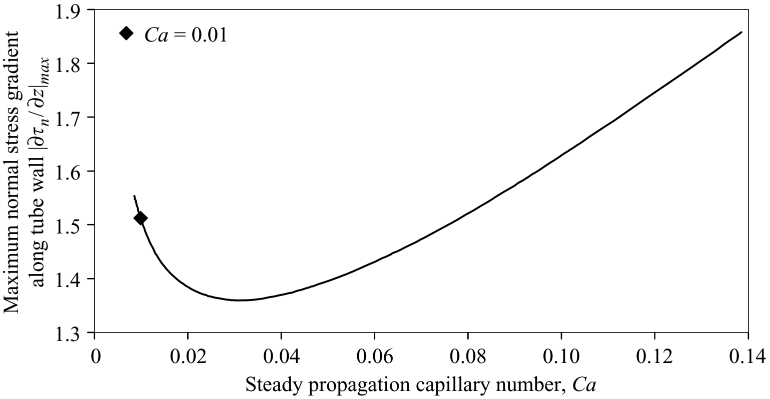

FIGURE 8. Maximum normal stress gradient magnitude $|\partial\tau_n/\partial z|_{max}$ along tube wall, steady-state bubble propagation.

section, we focus on the implications of these flow characteristics on the mechanical stresses that exist on the tube wall. As we will demonstrate, these stress fields are highly dependent on the flow parameters, which exhibit both spatial and temporal dependence. Specifically, we consider the normal stress gradient (§ 5.1) and shear stress (§ 5.2) along the tube wall. These responses are of fundamental interest and may also be of physiological significance, particularly in relation to pulmonary airway reopening, because these stresses (in particular, the normal-stress gradient), may damage tissues in the lung and exacerbate ventilation-induced lung injury.

5.1. *Normal stress gradient*

Magnitude

Our interest in the normal stress gradient stems from its importance in damage emanating from the reopening of fluid-occluded airways. Bilek *et al.* (2003) and Kay *et al.* (2004) demonstrated that an increased normal stress gradient $\partial\tau_n/\partial z$ along a channel wall is directly correlated to increased epithelial cell mortality. Those studies focused on very small values of Ca ($2.7 \times 10^{-5} \leqslant Ca \leqslant 6.8 \times 10^{-4}$), and showed that a decrease in Ca resulted in an increase in $\partial\tau_n/\partial z$ (corresponding to increased cell damage). Figure 8 shows that $\partial\tau_n/\partial z$ is a minimum along the tube wall under steady reopening conditions near $Ca = 0.03$. $\partial\tau_n/\partial z$ increases with decreasing Ca for $Ca < 0.03$ because the film becomes very thin in the transition region between the bubble cap and the upstream uniform film. This introduces a very high resistance region that must be overcome by a large pressure gradient. In contrast, at high Ca the high resistance region is not significant because the film has thickened. Instead, the maximum pressure gradient is dictated by the Poiseuille flow downstream of the bubble tip. In airway reopening, we are concerned with $Ca < 10^{-2}$, so the regime of $Ca < 0.03$ was of interest. We therefore target our studies on low-Ca behaviour ($Ca_M = 0.01$) because this region is most relevant to physiological systems.

Figure 9 shows the maximum normal stress gradient along the wall at any point in the oscillatory cycle, $(|\partial\tau_n/\partial z|_{max})_{cycle}$ as a function of Ca_Ω for $Ca_M = 0.01$ and $A = 5$. This figure shows that the system exhibits a *quasi-steady* regime ($Ca_\Omega < Ca_M$, to the left of +) wherein $(|\partial\tau_n/\partial z|_{max})_{cycle}$ is approximated by the steady-state results shown in figure 8. The unsteady regime can be sub-divided into three regions:

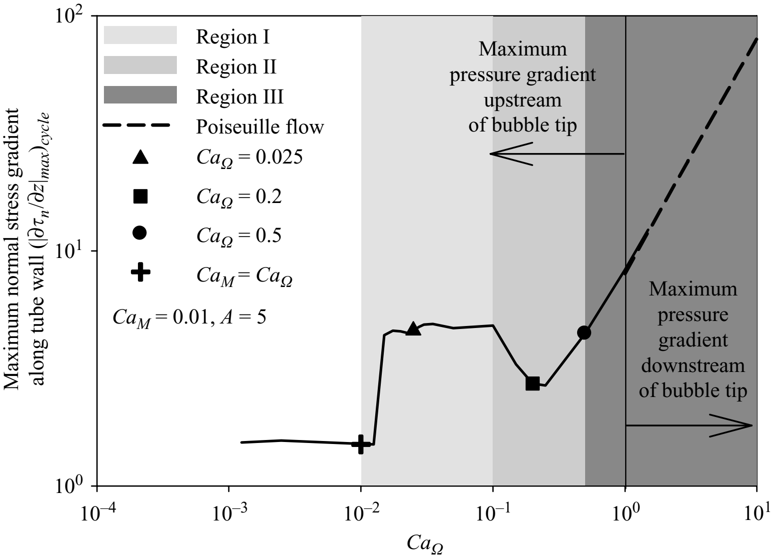

FIGURE 9. Maximum magnitude of the normal stress gradient along the tube wall at any point in the cycle $(|\partial\tau_n/\partial z|_{max})_{cycle}$ where $A = 5$ and $Ca_M = 0.01$. + indicates the onset of reverse flow ($Ca_\Omega = Ca_M$), data to the right-hand side of this point exhibits reverse flow. ––– indicates the region where the maximum normal stress gradient may be predicted by $(|\partial\tau_n/\partial z|_{max})_{cycle} = 8(Ca_M + Ca_\Omega)$. Light, medium, and dark grey indicate unsteady regimes I, II, and III, respectively.

Unsteady regime I. At low $Ca_\Omega (Ca_M < Ca_\Omega \leqslant 0.1)$, $(|\partial\tau_n/\partial z|_{max})_{cycle}$ is increased dramatically owing to interfacial flows near the bubble tip. The plateau region that occurs over $Ca_M < Ca_\Omega < 0.1$ diminishes with increasing Ca_M (data not shown).

Unsteady regime II. At moderate Ca_Ω $(0.1 < Ca_\Omega < 0.5)$, the system evolves from the low Ca_Ω plateau region to the high Ca_Ω response owing to local film thickening.

Unsteady regime III. At high Ca_Ω $(Ca_\Omega \geqslant 0.5)$, $(|\partial\tau_n/\partial z|_{max})_{cycle}$ is equivalent to the pressure gradient owing to the Poiseuille flow downstream of the bubble tip, following the form $(|\partial\tau_n/\partial z|_{max})_{cycle} = 8(Ca_M + Ca_\Omega)$.

Below, we elucidate the relationships between the normal stress gradient and interfacial geometry in the unsteady regime as they relate to the driving parameters A and Ω. In order to identify the interfacial characteristics that result in $(|\partial\tau_n/\partial z|_{max})_{cycle}$, we explore the behaviour of $|\partial\tau_n/\partial z|_{max}$ as a function of $Ca_Q(t)$ for $Ca_\Omega = 0.025$, 0.2 and 0.5, which represent unsteady regimes I–III, respectively. The time-dependent responses are provided in figure 10, where the symbols (▲, ■, ● as in figure 9) identify the specific portion of the cycle ($Ca_Q(t)$) associated with $(|\partial\tau_n/\partial z|_{max})_{cycle}$. Finally, we plot $\partial\tau_n/\partial z$ *vs.* z (figure 11*a*) and interfacial geometry at the $Ca_Q(t)$ (figure 11*b*) corresponding to $(|\partial\tau_n/\partial z|_{max})_{cycle}$, where the symbols (▲, ■, ●) precisely identify the location of $(|\partial\tau_n/\partial z|_{max})_{cycle}$.

Unsteady regime I. The time-dependent response in figure 10 at $Ca_\Omega = 0.025$ (solid line) corresponds to the sharp increase in the $(|\partial\tau_n/\partial z|_{max})_{cycle}$ shown in figure 9 (▲). This response demonstrates that $|\partial\tau_n/\partial z|_{max}$ varies substantially over the cycle, with the maximum value $(|\partial\tau_n/\partial z|_{max})_{cycle}$ (▲) occurring as a spike on the retracting stroke near $Ca_Q(t) = Ca_M - Ca_\Omega$. This magnitude far exceeds the $|\partial\tau_n/\partial z|$ that exists over the remainder of the cycle. The bubble tip geometry at this instant (figure 11*b*, solid

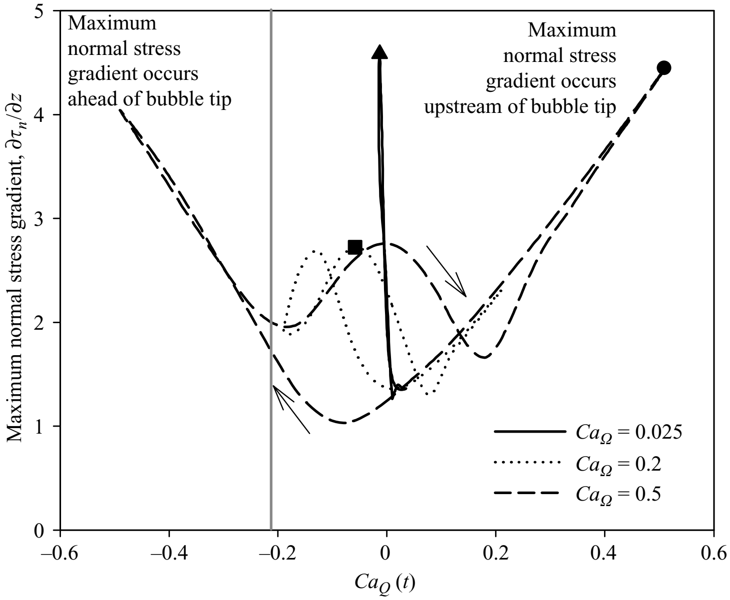

FIGURE 10. Normal stress gradient hysteresis loops for $Ca_M = 0.01$, $A = 5$. Location of $(|\partial\tau_n/\partial z|_{max})_{cycle}$ for ▲, $Ca_\Omega = 0.025$; ■, 0.2; ●, 0.5.

line) shows the extraordinary film thinning that occurs during this part of the reverse stroke. $\partial\tau_n/\partial z$ (figure 11*a*, solid line) demonstrates the extremely large normal-stress gradient that is exacerbated by this local film thinning. Therefore, the very large increase in $(|\partial\tau_n/\partial z|_{max})_{cycle}$ occurs as a result of very slow bubble retraction that induces a high-resistance region in the transition region between the bubble cap and thin film. The large magnitude of $\partial\tau_n/\partial z$ is consistent with the predictions of the stresses that exist in the leading edge of plug propagation, where the interface is moving in the reverse direction (Fujioka & Grotberg 2004).

Unsteady regime II. A local minimum in $(|\partial\tau_n/\partial z|_{max})_{cycle}$ occurs near $Ca_\Omega = 0.2$. The time-dependent response (figure 10) demonstrates that this increase in frequency modifies $|\partial\tau_n/\partial z|_{max}$ substantially. Local maxima occur at several points in the cycle, but the absolute maximum $(|\partial\tau_n/\partial z|_{max})_{cycle}$ occurs near $Ca_Q = -0.06$ (■). It is evident from the interfacial geometry (figure 11*b*, dotted line) that this marked reduction in $|\partial\tau_n/\partial z|_{max}$ occurs because oscillation has caused the film to thicken, which is consistent with figure 7*b*.

Unsteady regime III. With $Ca_\Omega = 0.5$, figure 10 shows that $|\partial\tau_n/\partial z|_{max}$ has local maxima occurring at velocity extrema and at $Ca_Q = 0$. $(|\partial\tau_n/\partial z|_{max})_{cycle}$ (●) occurs at the maximum forward velocity. At this rate, the film has thickened substantially (figure 11*b*), but the normal stress gradient remains very large owing to the elevated velocity that occurs from the high Ca_Ω. This corresponds to the large-Ca_Q behaviour in figure 9 (●). In this regime, $(|\partial\tau_n/\partial z|_{max})_{cycle}$ is equivalent to the Poiseuille viscous pressure gradient in the tube downstream of the bubble tip, following the form $(|\partial\tau_n/\partial z|_{max})_{cycle} = 8(Ca_M + Ca_\Omega)$. This relationship is provided by in figure 9.

Spatial and temporal behaviour

Bilek *et al.* (2003) and Kay *et al.* (2004) have demonstrated that the normal stress gradient is the mechanical stimulus that leads to cellular membrane disruption caused

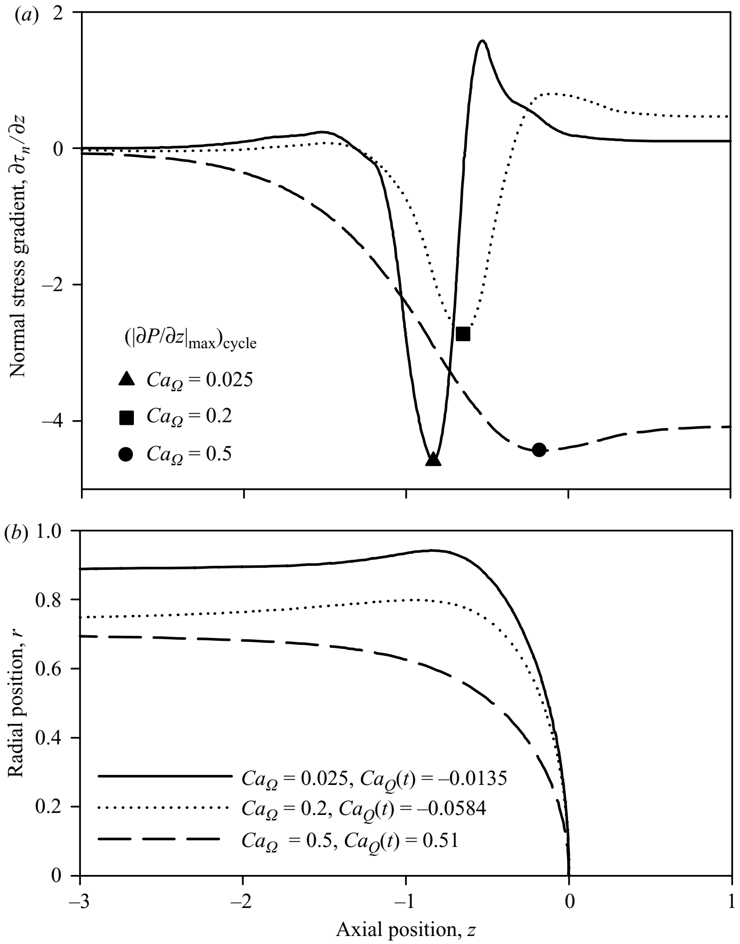

FIGURE 11. Normal stress gradient $\partial\tau_n/\partial z$ (*a*) and interfacial geometry (*b*) occurring at $(|\partial\tau_n/\partial z|_{max})_{cycle}$ for $Ca_M = 0.01$, $A = 5$. Symbols identify the location of $(|\partial\tau_n/\partial z|_{max})_{cycle}$ and correspond to those in figures 9 and 10.

by a finger of air passing over epithelial cells in a fluid-filled channel. In this subsection, we investigate the implications of the temporal and spatial variation of $\partial\tau_n/\partial z$, which leads to the complex signature described in figure 12(*a*, *c*).

In figure 12(*a*) we provide the time-dependent $\partial\tau_n/\partial z$ at a point fixed on the tube wall for $Ca_\Omega = 0.2$ and $A = 1$. Initially, this point is downstream of the bubble tip and experiences the gradient induced by the Poiseuille velocity profile. As the bubble tip approaches the fixed point (position decreasing to zero in figure 12*b*), $\partial\tau_n/\partial z$ is modified from pure oscillation as the interfacial $\partial\tau_n/\partial z$ sweeps across the cell (see figure 11*a* for an example of $\partial\tau_n/\partial z$ at one instant). In this low-amplitude high-frequency scenario, the bubble tip repeatedly passes over the fixed point, greatly increasing the potential for trauma. After the bubble tip has passed over the fixed point, the high-resistance transition region induces a large-magnitude time-dependent stress. For example, near $t = 14$, the magnitude of $\partial\tau_n/\partial z$ is at a maximum, and is qualitatively associated with the local film-thinning and high-resistance region that exists during the reverse flow. With increased t, the fixed point resides solely beneath

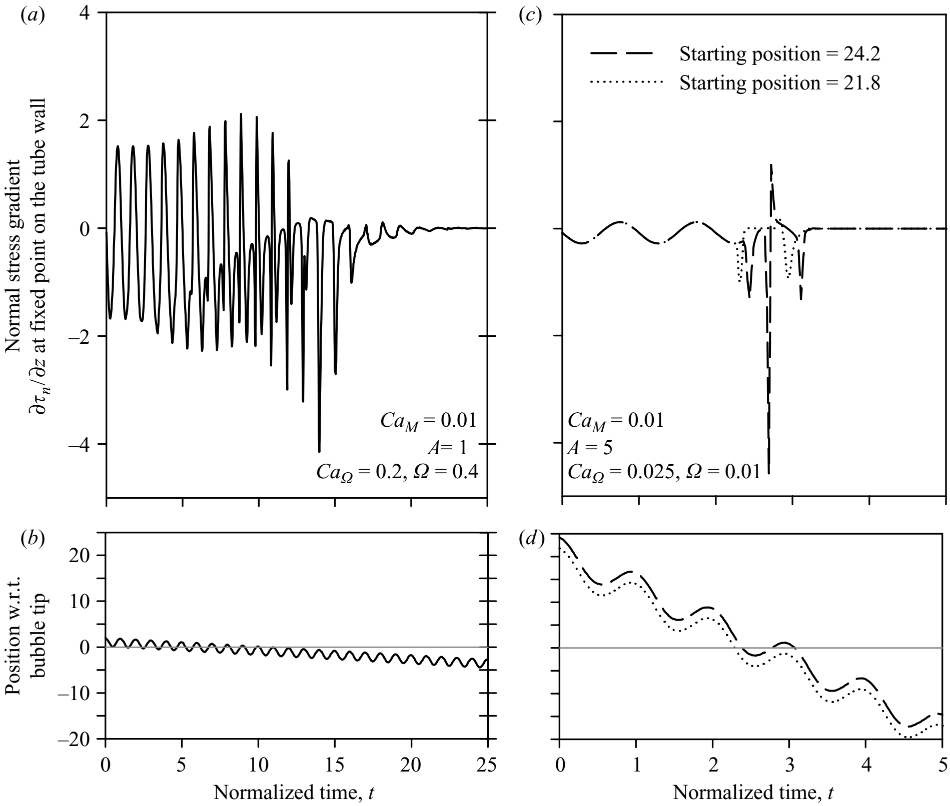

FIGURE 12. Normal stress gradient $\partial\tau_n/\partial z$ at a point fixed on the tube wall (*a,c*) and position with respect to the bubble tip (*b,d*). Time is normalized so that oscillations have a period of 1.

a nearly uniform thin film. Only a constant τ_n exists from the radial component of the bubble curvature, $\partial\tau_n/\partial z \sim 0$.

To explore the spatial dependency of the stress field, we consider the magnitude of $\partial\tau_n/\partial z$ affecting two points separated by a small distance ($z = 24.2$ and 21.8) at $A = 5$ and $Ca_\Omega = 0.025$ (figure 12*c*). This small variation in location results in significantly different transient $\partial\tau_n/\partial z$ during the time at which the bubble tip is passing over the points. This response occurs because each point on the wall is associated with different profiles of the time-dependent stress-field as a result of the Lagrangian translation of the bubble tip. As a result, adjoining points on the wall experience significantly different $\partial\tau_n/\partial z$ signatures. The wavelength of the spatial-dependency is approximately A, but would be slightly larger owing to the residual film which extends the stroke of the bubble tip according to figure 7.

When comparing figures 12(*a*) to 12(*c*), it is evident that both Ca_Ω and A greatly influence the stresses observed at a fixed point on the wall. For $Ca_\Omega = 0.2$ and $A = 1$ (figure 12*a*), the bubble passes a point on the wall 19 times, whereas for $Ca_\Omega = 0.025$ and $A = 5$ (figure 12*c*), the bubble passes by only three times. High frequency causes a region of the wall to experience more frequent exposure to the bubble tip, whereas increasing A leads to an extended range of bubble motion. As a result, high amplitudes and high frequency may induce repeated trauma.

5.2. Shear stress

Bilek *et al.* (2003) and Kay *et al.* (2004) demonstrate that normal stress gradient, not shear stress (τ_t) is primarily responsible for cellular damage in a simplified model of airway reopening. Nevertheless, other systems (i.e. epithelial cells in the vasculature) demonstrate effects that are triggered by τ_t. For this reason, we consider the relationship between τ_t and the flow parameters of our system. In the range investigated ($10^{-1} > Ca_M > 10^{-2}, 5 > Ca_\Omega > 0.00025$), a strong linear correlation ($R^2 \geqslant 0.999$) exists between the maximum $Ca_Q(t) = Ca_\Omega + Ca_M$ and the maximum shear stress $(\tau_t)_{max}$ along the tube wall at any point in the oscillatory cycle:

$$(\tau_t)_{max} = 4(Ca_\Omega + Ca_M). \tag{5.1}$$

We find that $(\tau_t)_{max}$ occurs upstream of the bubble tip only at low reopening velocities ($Ca_\Omega + Ca_M < 0.3$). Note that the linear relationship between $(\tau_t)_{max}$ and the maximum $Ca_Q(t)$ is likely to exist only at large $Ca_Q(t)$; the results of Bilek *et al.* (2003) demonstrate a weaker dependence with reducing Ca.

6. Limitations

In the model investigated herein we assume Stokes flow with time-dependent forcing and interfacial response dictated by the KBC (§ 3.4). In order to investigate the validity of the Stokes flow hypothesis, we rescale the Navier–Stokes equations with velocity and time scales relevant to system forcing. Scaling the Navier–Stokes equation with $u^* = \tilde{U}_{tip} u$ and $t^* = (1/\omega)t$ yields

$$\alpha^2 \frac{\partial \boldsymbol{u}}{\partial t} + Re(\boldsymbol{u} \cdot \nabla)\boldsymbol{u} = -\frac{1}{Ca_U}\nabla P + \nabla^2 \boldsymbol{u}, \tag{6.1}$$

where $Ca_U = \mu \tilde{U}_{tip}/\gamma$. The Womersley parameter α, describing the unsteady nature of the system, is equal to

$$\alpha = R\sqrt{\frac{\omega}{\nu}}, \tag{6.2}$$

where ν is the kinematic viscosity. The Reynolds number Re, the ratio of inertial to viscous forces, is defined as

$$Re = \frac{R\tilde{U}_{tip}}{\nu}. \tag{6.3}$$

Since the present investigation considers a balance between pressure and viscous interactions which ignores temporal and convective acceleration (2.3), Stokes flow is an appropriate approximation if the following conditions are satisfied:

$$\alpha^2 Ca_U \ll 1, \quad \alpha^2 \ll 1, \quad Re\, Ca_U = We \ll 1, \quad Re \ll 1. \tag{6.4}$$

Here the Weber number $We = ReCa$ represents the ratio of inertial forces to surface tension.

The Womersley parameter (α) describes the balance between unsteady inertial and viscous effects. For $\alpha < 1$, the downstream flow is quasi-steady and maintains a nearly parabolic profile. As α is increased, the downstream flow profile will assume a more plug-like configuration and become increasingly out of phase with the driving pressure gradient. In this study we assume the flow profile downstream of the bubble is parabolic, valid when $\alpha < 1$.

Heil (2001) systematically investigated the effect of Re on steady air finger propagation through a rigid channel. It was shown that variations in Re produced small variations in residual film thickness and significant changes in bubble tip pressure drop and flow field. Closed vortices were observed downstream of the bubble tip, not present in Stokes simulations. In the present investigation we neglect these inertial effects, and it is plausible that these may become significant at $Re > 1$. The present study therefore provides the baseline from which inertial effects can be investigated.

While our computational methods have provided a robust means for exploring a range of parameters, at high Ω and low Ca_M numerical difficulties may interfere with the solution process. In particular, the boundary-element method may suffer from poor accuracy when two boundaries are in very close proximity. This can occur at low Ca_M because the exceedingly thin film results in adjacent boundaries being separated by very small distances ($r < 0.05$). As a result, the time-dependent solver (DLSODES, § 3.5) may fail to converge at the specified error tolerances and iteration limits. To investigate this range of parameters, one could increase the level of Gauss quadrature for integration of the boundary integral equations (A3).

7. Conclusions

In this paper, we investigate the pulsatile motion of a finger of air propagating within a rigid tube filled with a viscous Newtonian fluid. We present a two-dimensional axisymmetric model incorporating the boundary-element method coupled to lubrication theory in the upstream thin-film region, driven by pulsatile flow at the downstream boundary.

We consider the time-dependent behaviour of the flow field and bubble geometry throughout the course of the oscillatory cycle. The behaviour of this system is approximated well by steady-state responses until the system enters the unsteady regime, $Ca_\Omega > Ca_M$. We explore ΔP_{tip}, κ_{tip}, U_{tip} and β throughout the cycle. We find that ΔP_{tip} may be estimated accurately ($(\Delta P_{tip})_{ext}$) from the pressure measured downstream of the bubble tip after correction for the viscous losses between the measuring point and the bubble tip. This relationship holds true far into the unsteady regime ($Ca_\Omega < 10Ca_M$) and suggests that $(\Delta P_{tip})_{ext}$ may be used in experimental investigation. Furthermore, we find that an increase in Ca_Ω increases the residual film $(1 - \bar{\beta})$ that is associated with a significant increase in $\bar{U}_{tip}$. Even though $\bar{\beta}$ increases during dynamic oscillation, extreme film thinning may occur at instances in the cycle. This, in turn, is correlated with a highly dynamic stress field which has temporal and spatial characteristics that may have implications for pulmonary airway damage associated with ventilator-induced lung injury. Further work will investigate the influence of coupling surfactant physicochemical hydrodynamics to this system, which may allow the predication of optimal ventilation strategies for the treatment of obstructive pulmonary disease.

The authors would like to thank Rene Salmon, Anne-Marie Jacob, and David Halpern for their assistance with this work. Computations were performed at the Center for Computational Science at Tulane University. This study was supported by NASA grant NAG3-2734, Louisiana Board of Regents graduate fellowships for B. J. S. and NIH grants R01-HL81266 and P20-EB001432.

Appendix A. Boundary element method (BEM)

The boundary-element method (BEM) is used to resolve the flow field near the bubble tip, as shown in figures 1 and 2. Ladyzhenskaya (1963) showed that

$$u_k(\boldsymbol{x}) = \int_S T_{ik}(\boldsymbol{x}, \boldsymbol{y}) u_i \, \mathrm{d}S - \frac{1}{Ca} \int_S U_{ik}(\boldsymbol{x}, \boldsymbol{y}) \tau_i \, \mathrm{d}S, \tag{A 1}$$

where T_{ik} and U_{ik} are the traction and velocity kernels, u_i is the velocity vector, and τ_i is the traction vector $\tau = \sigma_{fluid} \cdot \hat{\boldsymbol{n}}$. The axisymmetric form of the kernels used in this simulation may be found in Becker (1992, pp. 132–135 and Appendix D). Integrals are evaluated over positions $\boldsymbol{y}$ that describe the boundary $\boldsymbol{S}$. The solution vector $u_k = f(\boldsymbol{x})$ describes points $\boldsymbol{x}$ within the bounded domain. Near the boundary of the domain (A 1) is rewritten as

$$c_{ik} u_k(\boldsymbol{x}) = \int_S T_{ik}(\boldsymbol{x}, \boldsymbol{y}) u_i \, \mathrm{d}S - \frac{1}{Ca} \int_S U_{ik}(\boldsymbol{x}, \boldsymbol{y}) \tau_i \, \mathrm{d}S, \tag{A 2}$$

where c_{ik} accounts for the stress discontinuities occurring at the boundary. To implement this formulation, numerically the axisymmetric domain is discretized into N_{elm} 3-node quadratic elements as shown in figure 2. Note that it is unnecessary to discretize the centreline because this edge is not a boundary; instead it is an axis of rotation. When the axisymmetric domain is revolved about this axis, the fluid component is completely enclosed (and defined in the BEM) by surfaces 1–4.

Four degrees of freedom (DOF) exist at each BEM node: u_r, u_z, τ_r, τ_z. Velocity (u) and/or stress (τ) boundary conditions are applied on two of the four degrees of freedom. Nodes adjacent to two surfaces (figure 2) have four DOF for each surface, as discussed in Zimmer *et al.* (2005). The discrete formulation of (A 2)

$$C_{ki} U_i(\boldsymbol{x}) - \sum_{m=1}^{N_{elm}} \int_{S_m} T_{ik}(\boldsymbol{x}, \boldsymbol{y}) u_i \, \mathrm{d}S_m = -\frac{1}{Ca} \sum_{m=1}^{N_{elm}} \int_{S_m} U_{ik}(\boldsymbol{x}, \boldsymbol{y}) \tau_i \, \mathrm{d}S_m, \tag{A 3}$$

is then evaluated for each node, where S_m represents the boundary of element m. Numeric evaluation of the integrands in (A 3) for each element using standard Gaussian quadrature techniques yields

$$\boldsymbol{T}\boldsymbol{w} = \boldsymbol{U}\tilde{\boldsymbol{t}}. \tag{A 4}$$

The matrices $\boldsymbol{T}$ and $\boldsymbol{U}$ are of size $2N \times 2N$ and $2N \times 3N$ respectively, where N is the number of nodes. The vector $\boldsymbol{w}$ contains the velocities in the form $w_{2j-1} = u_{zj}$, $w_{2j} = u_{rj}$ and $\tilde{t}$ contains stress data $\tilde{t}_{2j-1} = \tau_{zj}$ and $\tilde{t}_{2j} = \tau_{rj}$, where and $j = 1, 2, \ldots, N$. $\boldsymbol{U}$ is $2N \times 3N$ so that two stresses may defined at the corner nodes. Either the velocity or stress is known at each corner. Equation (A 4) is arranged into the $\boldsymbol{A}x = b$ form where $\boldsymbol{A}$ is $2N \times 2N$, x is $2N$ and contains the unknown velocities and stresses, and b hold the known velocities and stresses obtained from the boundary conditions, and unknown velocities and stresses are identified through Gaussian elimination. When the solution at the boundary has been obtained, (A 1) is used to determine the internal velocity field.

Appendix B. Boundary conditions, BEM region

Region	u_r	u_z	τ_r	τ_z
Surface 1	0	$2Ca(1-r^2)$	–	–
Surface 1-2 corner on surface 1	–	0	$-4CaR$	–
Surface 1-2 corner on surface 2	0	–	–	$-4CaR$
Surface 2	0	0	–	–
Surface 2-3 corner on surface 2	0	–	–	$\left(\frac{\kappa_z}{2}\right)\left(r-\frac{r_{men}^2}{r}\right)$
Surface 2-3 corner on surface 3	–	0	$-\left(\frac{\kappa_z}{2}\right)\left(r-\frac{r_{men}^2}{r}\right)$	–
Surface 3	–	$\frac{\kappa_z}{2}\left(\frac{(r^2-1)}{2}-r_{men}^2\ln[r]\right)$	$-\left(\frac{\kappa_z}{2}\right)\left(r-\frac{r_{men}^2}{r}\right)$	–
Surface 3-4 corner on surface 3	–	$\frac{\kappa_z}{2}\left(\frac{(r^2-1)}{2}-r_{men}^2\ln[r]\right)$	0	–
Surface 3-4 corner on surface 4	–	–	$-\kappa n_r$	$-\kappa n_z$
Surface 4	–	–	$-\kappa n_r$	$-\kappa n_z$

TABLE 1. Boundary conditions.

REFERENCES

BECKER, A. A. 1992 *The Boundary Element Method in Engineering: A Complete Course.* McGraw-Hill.

BILEK, A. M., DEE K. C. & GAVER III, D. P. 2003 Mechanisms of surface-tension-induced epithelial cell damage in a model of pulmonary airway reopening. *J. Appl. Physiol.* **94**, 770–783.

BRETHERTON, F. P. 1961 The motion of long bubbles in tubes. *J. Fluid Mech.* **10**, 166–188.

COX, B. G. 1962 On driving viscous fluid out of a tube. *J. Fluid Mech.* **14**, 81–96.

FAIRBROTHER, F. & STUBBS, A. E. 1935 Studies in electroendosmosis. Part VI. The bubble-tube method of measurements. *J. Chem. Soc.* **1**, 527–529.

FUJIOKA, H. & GROTBERG, J. B. 2004 Steady propagation of a liquid plug in a 2d-channel. *Trans. ASME* K: *J. Biomech. Engng* **126**, 567–577.

FUJIOKA, H. & GROTBERG, J. B. 2005 Steady propagation of a surfactant laden liquid plug in a 2d-channel. *Phys. Fluids* **17**, 082102.

GAVER III, D. P, SAMSEL, R. W. & SOLWAY, J. 1990 Effects of surface tension and viscosity on airway reopening. *J. Appl. Physiol.* **69**, 74–85.

GAVER III, D. P, HALPERN, D, JENSEN O. E. & GROTBERG, J. B. 1996 The steady motion of a semi-infinite bubble through a flexible-walled channel. *J. Fluid Mech.* **319**, 25–65.

GAVER III, D. P., JACOB A.-M., BILEK, A. M. & DEE, K. C. 2006 The significance of air-liquid interfacial stresses on low-volume ventilator-induced lung injury. In *Ventilator-Induced Lung Injury* (ed. D. Dreyfuss, G. Saumon & R. D. Hubmayr), pp. 157–205. Taylor and Francis.

GHADIALI, S. N. & GAVER III, D. P. 2003 The influence of non-equilibrium surfactant dynamics on the flow of a semi-infinite bubble in a rigid cylindrical capillary tube. *J. Fluid Mech.* **478**, 165–196.

GHADIALI, S. N., HALPERN D. & GAVER III, D. P. 2001 A dual-reciprocity boundary element method for evaluating bulk convective transport of surfactant in free-surface flows. *J. Comput. Phys.* **171** 534–559.

GIAVEDONI, M. D. & SAITIA, F. A. 1997 The axisymmetric and plane cases of a gas phase steadily displacing a Newtonian fluid – a simultaneous solution of governing equations. *Phys. Fluids* **9**, 2420–2428.

GROTBERG, J. B. 2001 Respiratory fluid mechanics and transport processes. *Annu. Rev. Biomed. Engng.* **3**, 421–457.

HALPERN, D. & GAVER III, D. P. 1994 Boundary element analysis of the time-dependent motion of a semi-infinite bubble in a channel. *J. Comput. Phys.* **115**, 366–375.

HAZEL, A. L. & HEIL, M. 2003 Three-dimensional airway reopening: the steady propagation of a semi-infinite bubble into a buckled elastic tube. *J. Fluid Mech.* **478**, 47–70.

HAZEL, A. L. & HEIL, M. 2006 Finite-Reynolds-number effects in steady, three-dimensional airway reopening. *Trans. ASME* K: *J. Biomed. Engng* **128**, 573–578.

HEIL, M. 2000 Finite Reynolds number effects in the propagation of an air finger into a liquid-filled flexible-walled channel. *J. Fluid Mech.* **424**, 21–44.

HEIL, M. 2001 Finite Reynolds number effects in the bretherton problem. *Phys. Fluids* **13**, 2517–2521.

INGHAM, D. B., RITCHIE, J. A. & TAYLOR, C. M. 1992 The motion of a semi-infinite bubble between parallel plates. *Z. Angew. Math. Phys.* **43**, 191–206.

JUEL, A. & HEAP, A. 2006 The reopening of a collapsed fluid-filled elastic tube. *J. Fluid Mech.* **572**, 287–310.

KAY, S. S., BILEK, A. M., DEE, K. C. & GAVER III, D. P. 2004 Pressure gradient, not exposure duration, determines the extent of epithelial cell damage in a model of pulmonary airway reopening. *J. Appl. Physiol.* **97**, 269–276.

LADYZHENSKAYA, O. A. 1963 *The Mathmatical Theory of Viscous Incompressible Flow*. Gordon and Breach.

LU, W.-Q. & CHANG, H.-C. 1988 An extension of the biharmonic boundary integral method to free surface flow in channels. *J. Comput. Phys.* **77**, 340–360.

PARK, C. M. & HOMSY, G. W. 1984 Two-phase displacement in hele-shaw cells: theory. *J. Fluid Mech.* **139**, 291–308.

PERUN, M. L. & GAVER III, D. P. 1995*a* An experimental model investigation of the opening of a collapsed untethered pulmonary airway. *Trans. ASME* K: *J. Biomech. Engng* **117**, 245–253.

PERUN, M. L. & GAVER III, D. P. 1995*b* The interaction between airway lining fluid forces and parenchymal tethering during pulmonary airway reopening. *J. Appl. Physiol.* **75**, 1717–1728.

RAME, E. 2007 The stagnation point in marangoni-thickened landau-levich type flows. *Phys. Fluids* **19**, 078102.

RATULOWSKI, J. & CHANG, H.-C. 1989 Transport of gas bubbles in capillaries. *Phys. Fluids* A **1**, 1642–1655.

REINELT, D. A. & SAFFMAN, P. G. 1985 The penetration of a finger into a viscous fluid in a channel and tube. *SIAM J. Sci. Stat. Comput.* **6**, 542.

SHEN, E. I. & UDELL, K. S. 1985 A finite element study of low reynolds number two-phase flow in cylindrical tubes. *Trans. ASME* E: *ASME J. Appl. Mech.* **52**, 253–256.

STEBE, K. J. & BARTHES-BIESEL, D. 1995 Marangoni effects of adsorption –desorption controlled surfactants on the leading edge of an infinitely long bubble in a capillary. *J. Fluid Mech* **286**, 25–48.

STEBE, K. J. & MALDARELLI, C. 1994 Remobilizing surfactant retarded fluid particle interfaces ii. controlling the surface mobility at interfaces of solutions containing surface active components. *J. Colloid Interface Sci.* **163**, 177–189.

WASSMUTH, F. LAIDLAW, W. G. & COOMBE, D. A. 1993 Calculation of Interfacial flows and surfactant redistribution as a gas/liquid interface moves between two parallel plates. *Phys. Fluids* A **5**, 1533–1548.

YAP, D. Y. K. & GAVER III, D. P. 1998 The influence of surfactant on two-phase flow in a flexible-walled channel under bulk equilibrium conditions. *Phys. Fluids* **10**, 1846–1863.

YAP, D. Y. K., LIEBKEMANN, W. D., SOLWAY, J. & GAVER III. D. P. 1994 The influence of parenchymal tethering on the reopening of closed pulmonary airways. *J. Appl. Physiol.* **76**, 2095–2105.

ZIMMER, M. E., WILLIAMS, H. A. R. & GAVER III, D. P. 2005 The pulsatile motion of a semi-infinite bubble in a channel: flow fields, and transport of an inactive surface-associated contaminant. *J. Fluid Mech.* **537**, 1–33.